Energy Advances

ROYAL SOCIETY OF CHEMISTRY

PAPER

View Article Online
View Journal | View Issue

Cite this: *Energy Adv.*, 2023, 2, 1905

An Fe_3O_4 based hole transport bilayer for efficient and stable perovskite solar cells†

Akbar Ali Qureshi,[abc] Emilia R. Schütz,[c] Sofia Javed,*[a] Lukas Schmidt-Mende[c] and Azhar Fakharuddin*[c]

Received 7th January 2023,
Accepted 26th September 2023

DOI: 10.1039/d3ya00014a

rsc.li/energy-advances

The hole transport layer (HTL) critically affects the photovoltaic performance and stability of metal halide perovskite solar cells (PSCs). So far, spiro-OMeTAD remains the most successful HTL; however, concerns remain regarding the stability of the PSCs using a spiro-OMeTAD based HTL. Herein, we report an inorganic–organic Fe_3O_4/spiro-OMeTAD bilayer HTL that not only shows a superior device performance than a pristine spiro-OMeTAD counterpart but also an enhanced shelf-life stability. The experimental results show that the inclusion of an Fe_3O_4 layer between the perovskite and the spiro-OMeTAD reduces the surface roughness, which in turn leads to the formation of a smooth and pin-hole free HTL. The bilayer HTL design improves charge extraction and also reduces the interfacial trap density, as demonstrated by steady-state and time-resolved photoluminescence and space charge limited current measurements, respectively. The Fe_3O_4/spiro-OMeTAD bi-layer HTL demonstrated significant enhancement in photovoltaic performance, such as 11% higher power conversion efficiency (PCE) than the reference device, and also exhibited long-term shelf-life stability by retaining 89% of its initial PCE after around 1300 hours. Our study proposes a simplistic strategy for the fabrication of efficient and stable PSCs by employing the inorganic–organic stack architecture of HTLs.

1. Introduction

Organic–inorganic metal halide perovskites with the general formula ABX_3 have been extensively investigated in solution-processed solar cells owing to their exceptional optoelectronic properties including long charge carrier lifetime, ambipolar transport, high carrier mobility, high absorption coefficient and defect tolerance.[1–5] An added benefit is the possibility to tune their bandgap from ultraviolet to near-infrared by compositional engineering, which opens up the possibility of their integration into tandem solar cell architecture.[6,7] Perovskite solar cells (PSCs) have reached a certified power conversion efficiency (PCE) of 25.8%[8] within a decade since their first reports in 2012 in solid state architectures. Despite the unprecedented increase in device performance, concerns regarding stability and toxicity might hinder their potential as future PV technology.[9,10] The instability in the PSCs stems from the intrinsic factors such as perovskite (defects, ion migration) and the properties of interfaces between perovskite and the surrounding charge selective layers, as well as external factors such as humidity, temperature, applied bias and oxygen.[11–15]

Charge transport materials, particularly the HTL, have been considered to be a crucial component in the PSCs that impact device performance and operational stability.[16–18] To date, PSCs in a regular n–i–p architecture have mostly employed the organic hole transport materials such as poly (3-hexylthiophene) (P3HT), poly(triarylamine) (PTAA), and 2,2′,7,7′-tetrakis(*N*,*N*-di-*p*-methoxyphenylamine)-9,9′-spirobifluorene (spiro-OMeTAD).[19–22] Amongst all these, spiro-OMeTAD remains the most commonly used HTL owing to the appropriate energy levels and ease of processing.[23,24] Obtaining high performing PSCs based on spiro-OMeTAD, however, requires the inclusion of hygroscopic dopants and additives such as lithium bis(trifluoromethanesulfonyl)imide (Li-TFSI), 4-*tert*-butylpyridine (*t*BP), and cobalt (Co-II) to enhance its hole mobility.[25,26] The inclusion of these dopants adversely impacts the device operational stability as these dopants, particularly Li-TFSi, are volatile and hygroscopic and Li has been shown to diffuse into the adjacent interfacing layer causing degradation.[27–29] The low thermal stability and high cost of these organic HTLs are not favorable and critically hinder the quest for stable and low-cost PSCs.[30–32] The dopant-free HTLs have also been explored, but still they suffer from low efficiencies and unveil poor reproducibility.[33]

[a] *School of Chemical & Materials Engineering, National University of Sciences & Technology, 44000, Islamabad, Pakistan. E-mail: sofia.javed@scme.nust.edu.pk*
[b] *Department of Mechanical Engineering, Bahauddin Zakariya University, 60000, Multan, Pakistan*
[c] *Department of Physics, University of Konstanz, 78464, Konstanz, Germany. E-mail: azhar-fakhar.uddin@uni-konstanz.de*

† Electronic supplementary information (ESI) available. See DOI: https://doi.org/10.1039/d3ya00014a

Recently, inorganic p-type metal oxide HTLs such as NiO_x, CuO_x, CuSCN, and $CuGaO_2$ have proven to be potentially stable, dopant-free, and low-cost alternatives to organic HTLs.[34–38] Moreover, the inorganic HTLs exhibit a higher thermal/chemical stability than their organic counterparts, transparency in the visible spectrum, and high mobility.[39,40] These inorganic HTLs are mostly compatible with the inverted p–i–n architecture due to their dispersion in polar solvents and high annealing temperature processing, which restricts their deposition on top of the perovskite layer.[41–43] Depositing these inorganic HTLs on the perovskite layer demands a further investigation for stable and efficient PSCs.[44] Magnetite (Fe_3O_4) is a p-type metal oxide semiconductor seldomly explored in the literature of PSCs and exhibits modest hole mobility, low cost, stability, and nontoxicity and offers facile synthesis. Moreover, the valence band of the Fe_3O_4 matches well with the spiro-OMeTAD and perovskite.[45] Fe_3O_4 has been mostly explored in polymer solar cells as a hole extraction material[46,47] and can also be applied as a low-cost and stable inorganic HTL in PSCs.

In this study, we demonstrate the beneficial effect of a bilayer HTL (Fe_3O_4/spiro-OMeTAD) on the photovoltaic performance and stability of triple-cation based planar n–i–p PSCs. A thin layer of Fe_3O_4 nanoparticles dispersed in toluene was deposited between the perovskite and spiro-OMeTAD layers without any further thermal treatment, which is expected to also prevent the Li ion diffusion from the spiro-OMeTAD layer. The bilayer HTL facilitates superior hole extraction and transport owing to the well-matched energy level with that of the perovskite layer, and enables the deposition of a more uniform spiro-OMeTAD layer atop. The Fe_3O_4/spiro-OMeTAD bilayer structure, which has never been reported in PSCs, results in 11% relative improved PCE in the PSCs compared to pristine spiro-OMeTAD based counterparts and also an improved shelf-life stability.

2. Experiment section

Materials

PbI_2 (99.99%) was purchased from TCI. The SnO_2 nanoparticle (15 wt %) dispersion was procured from Alfa Aesar. CsI (99%), $PbBr_2$ (99.9%), DMSO (99.8%), CB (99.8%), acetonitrile (ACN), *N*,*N*-DMF (99.8%), and 5 mg mL^{-1} Fe_3O_4 nanoparticles ($\sim$10 nm) dispersed in toluene were procured from Aldrich. MABr (99%) and FAI (99%) were purchased from Greatcell. Spiro-OMeTAD ($>$99%) and ITO-coated glass substrates with a sheet resistance of 15 Ω were obtained from Lumtec.

Fabrication of PSCs

ITO coated glass substrates were etched chemically using Zn powder and a 2 M diluted solution of HCL. The etched substrates were cleaned with soap water, distilled water, acetone, and IPA each for 15 min. The ITO substrates were dried under N_2 flow and subjected to O_2 plasma treatment for 7 min to remove any organic impurities on the ITO surface. The electron transport layer (ETL) was prepared by spin coating 80 μL SnO_2 diluted dispersion (2.67 wt%) at 3000 rpm at a ramp rate of 1000 rpm for 30 s following annealing in air at 150 °C for 30 min. The ETL-deposited ITO substrates were treated with UV-ozone for 20 min prior to deposition of the perovskite film. The triple cation perovskite solution was synthesized by dissolving 0.2 M $PbBr_2$, 1.1 M PbI_2, 0.2 M MABr, and 1 M FAI, in a mixed solvent of DMF : DMSO (4 : 1 by volume). First, the $PbBr_2$ and PbI_2 salts were mixed in DMF : DMSO at 100 °C for around 30 minutes. The solution was cooled down and poured into a glass vial containing MABr and FAI precursors. To this solution, 53 μL of 1.5 M CsI solution was added to attain the stoichiometry $Cs_{0.05}(FA_{0.83}MA_{0.17})_{0.95}Pb(I_{0.83}Br_{0.17})_3$ of triple cation perovskite or simply abbreviated as CsFAMA.[48] The perovskite precursor and HTL deposition were carried out in an N_2-filled glove box. 45 μL perovskite precursor solution was spin-coated at 1000 rpm for 10 s followed by spinning at 6000 rpm for 25 s. 200 μL CB (antisolvent) was dropped on the spinning substrate around 8 s before the end of the spin-coating process. The films were annealed at 120 °C for 10 min to complete the crystallization process. For bilayer HTL synthesis, an Fe_3O_4 dispersion (50 μL, 5 mg mL^{-1} in toluene) was spin-coated onto the annealed perovskite layer at 3000 rpm for 30 s at a ramp rate of 400 rpm. Finally, a spiro-OMeTAD solution (73 mg mL^{-1}) was prepared in CB with 28.8 μL TBP and 17.5 μL Li-TFSI as dopants. The solution was spin-coated (30 μL) atop the perovskite films at 4000 rpm (ramp 1000 rpm) for 40 s.[49] The device fabrication was completed by thermal evaporation of WO_3 (3 nm) as a buffer layer and Ag (100 nm) as a back contact under a vacuum below 7.5×10^{-6} mbar. The active area of the PSCs was demarcated (0.133 cm^2) using a shadow metal mask with all edges properly covered for a reliable measurement.

Thin films and device characterization

The crystallinity of the thin films was recorded using an X-ray diffractometer (Bruker D8 Advance). The surface morphology was analyzed by employing a scanning electron microscope (Zeiss Gemini 500 FESEM) and an atomic force microscope (Park NX 10 AFM). The optical properties of the thin films were investigated *via* UV-Vis-NIR spectrophotometer (Cary 5000). Steady-state photoluminescence (PL) and time-resolved photoluminescence (TRPL) measurements were performed with a fluorescence spectrometer (PicoQuant FluoTime 300) with a 404 nm laser source. The PSCs were measured with a home-made setup, which was calibrated with a Si reference diode (Fraunhofer ISE). Current–voltage (*J*–*V*) curves and maximum power point tracking (MPP) were recorded using a Keithley 2410 source meter under a simulated AM 1.5 G spectrum and KG5 filter. The solar cells were measured in forward and reverse scan directions (0 V to 1.2 V) with a step size of 0.01 V and a delay time of 100 ms. The external quantum efficiency (EQE) spectra were recorded by using a xenon light source equipped with a grating monochromator (LOT-Oriel Omni 300). The space charge limited current (SCLC) measurements were performed to assess charge carrier mobility and trap densities.

For the shelf-life test, the devices were stored in an inert atmosphere (N_2, room temperature) and measured inside a glovebox under an illumination intensity of 100 mW cm^{-2} (AM 1.5 G spectrum). The solar cells were measured in the scan direction (0 V to 1.2 V) with a step size of 0.01 V and a delay time of 100 ms.

3. Results and discussion

Fig. 1(a) shows the X-ray diffraction pattern of the Fe_3O_4 nanoparticles (average size: ~10 nm) dispersed in toluene and spin-coated on glass/ITO substrates. The 2θ peaks at 30.15°, 35.49°, 37.04°, 43.05°, 53.43°, 56.92°, and 62.55° were dispensed to (220), (311), (222), (400), (422), (511), and (440) crystallographic planes of the cubic crystal structure of magnetite (JCPDS: 89-3854). The peaks are sharp and highly crystalline with no phase of any impurity.

The surface morphology of Fe_3O_4 nanoparticles deposited on the ITO substrate was examined by SEM. A pinhole-free and smooth surface morphology was observed for the ITO/Fe_3O_4 thin film (Fig. 1(b)). The spherical-shaped nanoparticles are homogeneous and uniformly distributed with good surface coverage. The improved morphology may arise due to the high dispersibility of magnetite nanoparticles in toluene, which can be favorable for achieving high performance in PSCs. Furthermore, we did not observe any significant change in the transmittance of ITO after Fe_3O_4 deposition affirming that ITO/Fe_3O_4 also has high transmittance as manifested in Fig. 1(c), which can be helpful if Fe_3O_4 is to be used as a charge selective contact beneath the perovskite absorber layer. The absorbance of the thin film was studied by depositing CsFAMA, CsFAMA/spiro, and CsFAMA/Fe_3O_4/spiro over ITO/SnO_2 ETLs. From Fig. 1(d), all samples exhibited identical absorption similar to the pristine CsFAMA perovskite film. Fig. S1 (ESI†) shows the XRD patterns for single-layer spiro-OMeTAD and double-layer Fe_3O_4/spiro-OMeTAD deposited over ITO/SnO_2/CsFAMA thin films. Both patterns exhibit standard perovskite peaks around 14°.[48] No peak resulting from PbI_2 was observed in both patterns confirming perovskite stability under the unmodified and Fe_3O_4-modified HTLs.

The surface morphology of different HTLs such as Fe_3O_4, spiro-OMeTAD, and Fe_3O_4/spiro-OMeTAD bilayers, deposited on the ITO/SnO_2/CsFAMA perovskite was analyzed using scanning electron microscopy (SEM) and atomic force microscopy (AFM) and the corresponding micrographs are depicted in Fig. 2. The CsFAMA perovskite exhibited a dense and crack-free morphology on the SnO_2 ETL (Fig. 2(a)) and the root-mean-square (RMS) roughness value of 26.4 nm (Fig. 2(e)). The Fe_3O_4 nanoparticle layer atop the CsFAMA perovskite showed a uniform thin layer (Fig. 2(b)) with lower roughness (25.8 nm) as compared to the pristine perovskite layer (Fig. 2(f)). The smooth overlayer with a lower surface roughness is more favorable in

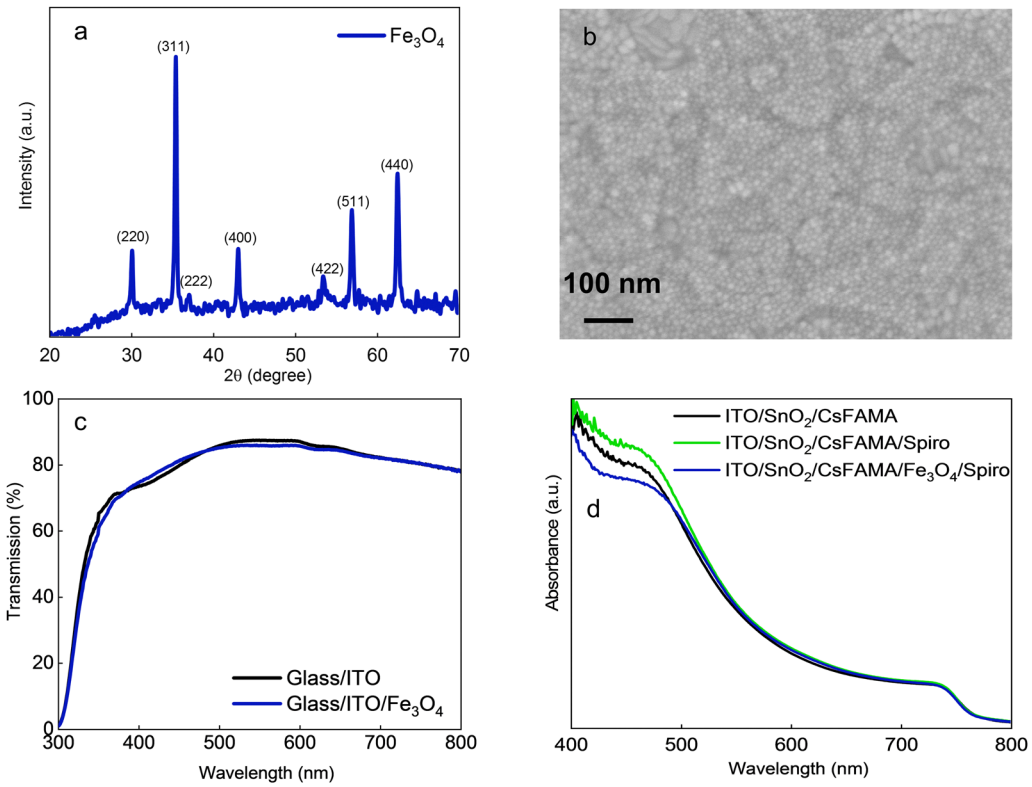

Fig. 1 X-ray diffraction pattern of Fe_3O_4 nanoparticles (a), top-view SEM images of the Fe_3O_4 nanoparticle spin-coated thin film on ITO (b), transmission spectra of pristine glass/ITO and glass/ITO/Fe_3O_4 thin films (c), and absorption spectra of CsFAMA, CsFAMA/spiro-OMeTAD and CsFAMA/Fe_3O_4/spiro-OMeTAD thin films deposited on ITO/SnO_2 ETLs (d).

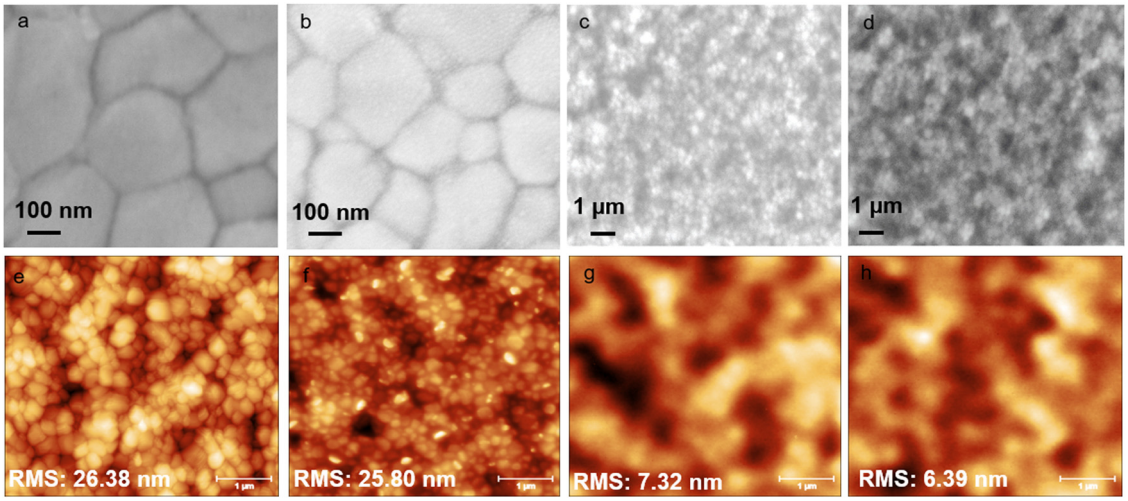

Fig. 2 Top view SEM images of ITO/SnO_2/CsFAMA (a), ITO/SnO_2/CsFAMA/Fe_3O_4 (b), ITO/SnO_2/CsFAMA/spiro (c), and ITO/SnO_2/CsFAMA/Fe_3O_4/spiro (d). AFM images of ITO/SnO_2/CsFAMA (e), ITO/SnO_2/CsFAMA/Fe_3O_4 (f), ITO/SnO_2/CsFAMA/spiro (g), and ITO/SnO_2/CsFAMA/Fe_3O_4/spiro (h).

enhancing the ohmic contact, which can improve device performance.[40] A comparison of the morphologies of the spiro-OMeTAD and Fe_3O_4/spiro-OMeTAD HTLs suggests that the spiro-OMeTAD layer contains various holes (Fig. 2(c) and (g)), probably due to the addition of Li-TFSI and tBP dopants, which can provide pathways for the air or oxygen to penetrate inside the perovskite layer resulting in lower stability and diminished photovoltaic performance of the PSCs.[43] However, the spiro-OMeTAD layer on the Fe_3O_4 layer does not possess any significant holes despite the dopant inclusion suggesting the formation of a more uniform and pin-hole free layer (Fig. 2(d) and (h)). Such a layer can lead to the fabrication of more stable, efficient, and reproducible PSCs. The Fe_3O_4/spiro-OMeTAD bilayer HTL also showed a lower rms roughness of

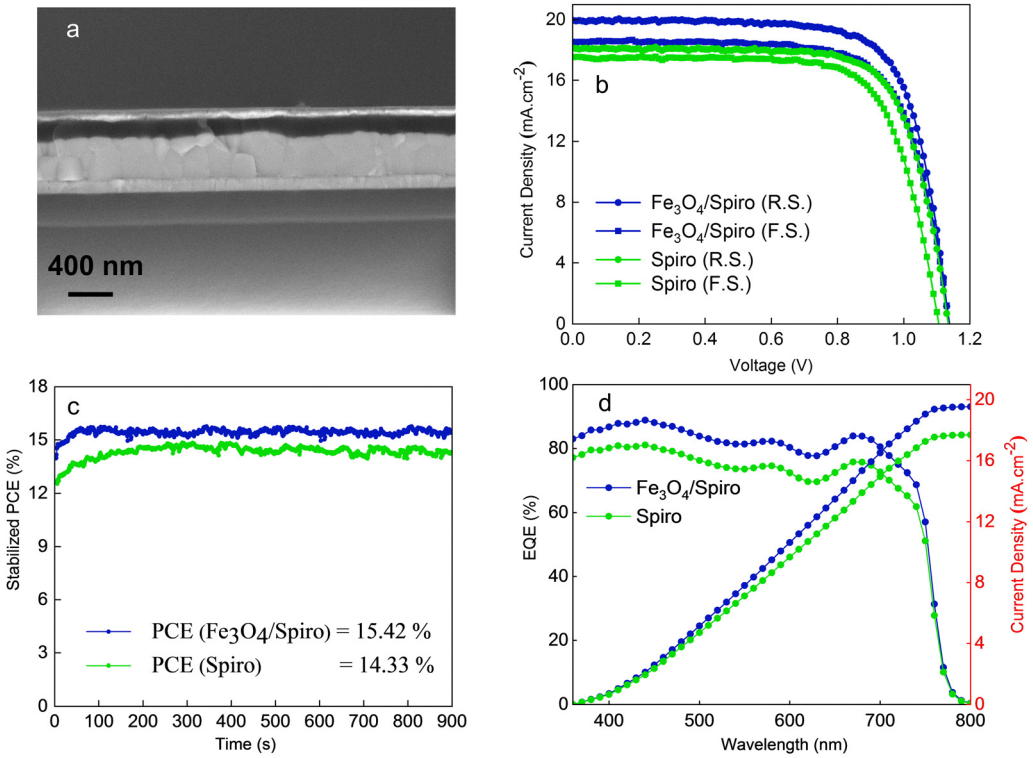

Fig. 3 Cross-sectional SEM image of a complete PSC (a), the photovoltaic performance of bilayer HTL-based PSCs: (b) *J*–*V* curves of the perovskite devices using Fe_3O_4/spiro-OMeTAD and spiro-OMeTAD HTLs in forward and reverse scan, (c) maximum power points tracking of the PSCs, and (d) EQE spectra of the same.

Table 1 Photovoltaic parameters of perovskite devices using a bilayer Fe_3O_4/spiro-OMeTAD and pristine spiro-OMeTAD HTL

HTL	Scan direction	J_{SC} (mA cm^{-2})	V_{OC} (V)	FF (%)	PCE (%)
Fe_3O_4/spiro	RS	20.0	1.14	73.4	16.7
	FS	18.6	1.14	71.8	15.2
Spiro	RS	18.1	1.14	73.3	15.1
	FS	17.5	1.11	71.9	13.9

6.4 nm (Fig. 2(h)) compared to that of the pristine spiro-OMeTAD layer at rms roughness of 7.3 nm (Fig. 2(g)). The lower surface roughness is due to the formation of a uniform and flat Fe_3O_4 thin film, which can lead to the formation of a more favourable contact at the perovskite/HTL interface.

The PSC was fabricated in a regular n–i–p configuration ITO/SnO_2/CsFAMA/Fe_3O_4/spiro-OMeTAD/WO_3/Ag as manifested in Fig. S2(a) (ESI†). Fe_3O_4 nanoparticles (average size ~10 nm) dispersed in toluene (nonpolar) were spin-coated on the annealed perovskite layer. The use of toluene as a solvent is because nonpolar solvents do not induce degradation of the perovskite layer.[42] Fig. 3(a) shows the cross-section of the complete PSC. The Fe_3O_4 HTL is difficult to distinguish from cross-sectional images owing to its extremely thin thickness. The perovskite and spiro-OMeTAD layers are around 490 nm and 195 nm. Fig. 3(b) exhibits the current–voltage (*J–V*) characteristics of Fe_3O_4/spiro-OMeTAD and pristine spiro-OMeTAD HTL-based PSCs measured under standard conditions (AM 1.5G solar irradiation). The PSCs employing a bilayer HTL demonstrated an enhancement in photovoltaic parameters. The PCE of the Fe_3O_4/spiro-OMeTAD HTL-based device was increased from 15.07% (for PSCs employing pristine spiro-OMeTAD HTL) to 16.64%. The enhancement in the PCE primarily stems from a higher J_{SC} of 20.0 mA cm^{-2} (up from 18.1 for a reference PSC), as shown in Table 1. We also fabricated the pristine Fe_3O_4 HTL-based PSCs for comparison. Fig. S3 (ESI†) exhibits the light and dark *J–V* curves of Fe_3O_4-only HTL-based devices and the corresponding photovoltaic parameters are listed in Table S1 (ESI†). It is evident that the Fe_3O_4-only HTL shows a low PCE of 3.1%, primarily due to a low V_{OC} and low FF suggesting a higher recombination. The dark *JV* curves (Fig. S3, ESI†) indicate that although the Fe_3O_4 thin layer is favourable for a higher charge extraction (as evidenced from a higher injected current than a pristine spiro-OMeTAD HTL), it shows around 15 times higher leakage current. The high leakage current, which is due to the extremely thin film, is responsible for the higher recombination in the Fe_3O_4-only PSCs. However, when combined with the sipro-OMeTAD (in a bilayer HTL), the combination of both HTLs brings the best of both HTLs, *i.e.* the blocking capabilities of spiro-OMeTAD and charge extraction capabilities of the Fe_3O_4.

Fig. 3(c) shows the steady-state power output for the reference and the target devices. The MPP measurements exhibited a stabilized power output of 15.4% and 14.3% for Fe_3O_4/spiro-OMeTAD and spiro-OMeTAD HTLs-based devices, respectively, for 900 s (15 min). In another separate measurement, the device exhibited a steady state J_{SC} of 18.9 mA cm^{-2}, V_{OC} of 1.1 V, and

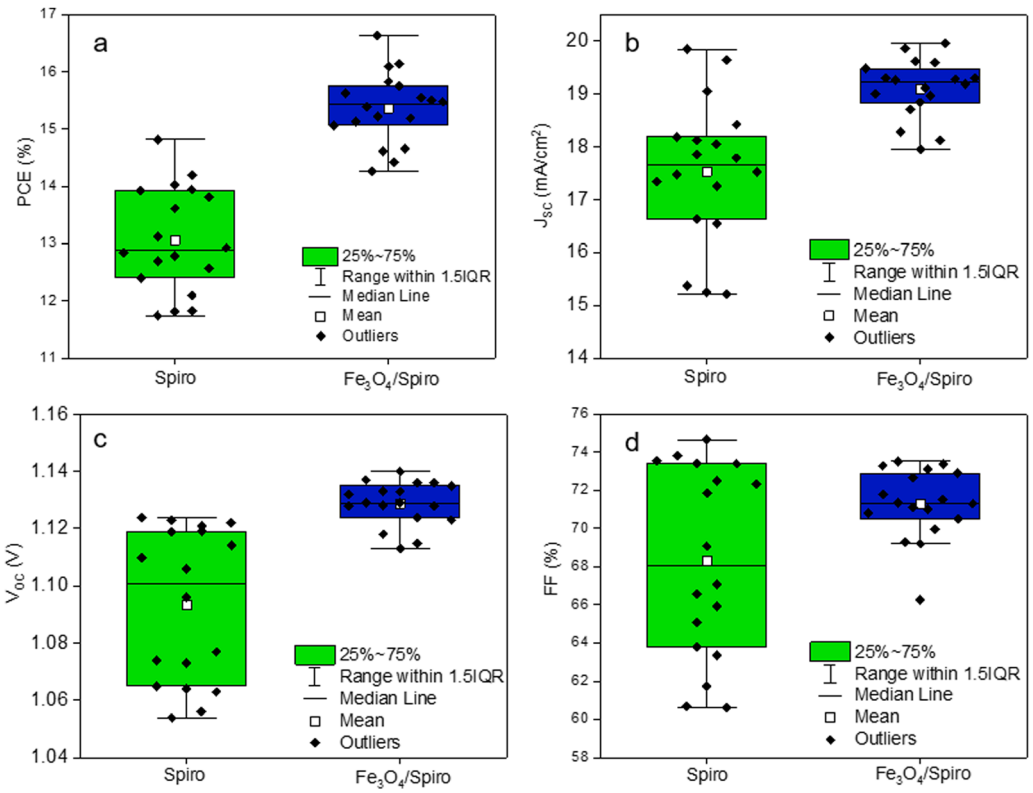

Fig. 4 Statistical analysis of photovoltaic parameters of the PSCs employing different HTLs (a) PCE, (b) J_{SC}, (c) V_{OC}, and (d) FF.

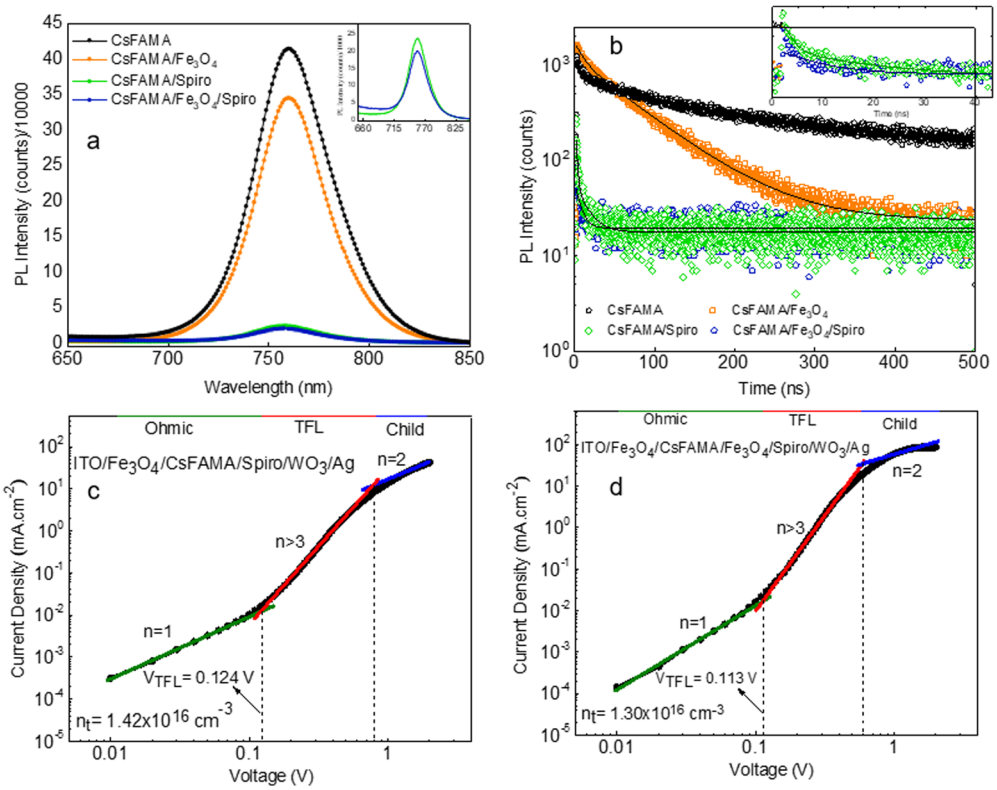

Fig. 5 Steady-state PL spectra of CsFAMA films with or without different HTLs (a), time-resolved PL spectra of CsFAMA films with or without different HTLs (b), SCLC measurement of hole-only devices with structure: ITO/Fe_3O_4/CsFAMA/spiro/WO_3/Ag structure-based device (c), and ITO/Fe_3O_4/CsFAMA/Fe_3O_4/spiro/WO_3/Ag (d).

stable PCE of 15.4% for 300 s (Fig. S4, ESI†). Fig. 3(d) depicts the EQE spectra of Fe_3O_4/spiro-OMeTAD and spiro-OMeTAD HTL-based PSCs. The integrated J_{SC} values for the modified and unmodified devices were 19.5 mA cm^{-2} and 17.7 mA cm^{-2}, respectively, confirming the enhanced charge extraction in the bilayer HTL-based PSCs. The integrated J_{SC} values were found to be around 2.5% less than those obtained from the *J–V* curves, which might be due to the difference in intensity of the light sources used for both measurements. To demonstrate the reproducibility of the PSCs, we show the *JV* data from 18 devices based on both HTLs (Fig. 4). The PSCs employing a bilayer HTL showed a narrow distribution of the PV parameters affirming a good reproducibility. The bilayer HTL containing PSCs showed an average PCE (15.37 ± 1.19%), J_{SC} (19.10 ± 1 mA cm^{-2}), V_{OC} (1.12 ± 0.02 V), and FF (71.28 ± 3.6%), which is higher than the PSCs employing pristine spiro-OMeTAD HTL (PCE of 13.06 ± 1.59%, J_{SC} 17.53 ± 2.3 mA cm^{-2}, V_{OC} 1.09 ± 0.03 V, and FF 68.3 ± 6%). The enhancement in PV parameters for the modified HTL-based devices is mainly attributed to enhanced charge extraction by the bilayer HTL leading to reduced charge recombination or could be due to interface passivation due to the thin magnetite layer. In addition, to optimize the processing conditions of the Fe_3O_4 layer, we fine tune the spin coating conditions, *i.e.* acceleration and spin coating process. The statistical results for the optimization processes are also displayed in Fig. S5 and S6 in the ESI.† The 400 rpm spinning acceleration at 3000 rpm for 30 s and three-step spin coating showed much better performance mainly due to better surface coverage of the thin layer of magnetite nanoparticles onto the perovskite layer.

The energy band level diagram is beneficial in getting insights about energy levels, band alignment, and charge extraction *via* different HTLs. As can be seen in Fig. S7 (ESI†), the valence band of Fe_3O_4 lies at around −5.3 eV, which is 100 meV lower than that of spiro-OMeTAD (−5.2 eV). The inclusion of an Fe_3O_4 thin layer is thus favorable in reducing the barrier for hole extraction from the perovskite.[45] The Fe_3O_4 interlayer can also improve the FF owing to improved ohmic contact. The mobility of charge carriers is also another key factor for fast carrier extraction and transfer. Fig. S8 (ESI†) depicts the SCLC measurement of the hole-only device with configuration (ITO/Fe_3O_4/WO_3/Ag). The SCLC measurements yield a mobility of Fe_3O_4 of 8.27 × 10^{-4} cm^2 V^{-1} s^{-1}, which is comparable to the reported mobility values of the pristine spiro-OMeTAD.

In order to validate the improved charge extraction in the bilayer HTL, steady-state photoluminescence (PL) and time-resolved photoluminescence (TRPL) measurements were carried out for the perovskite film without a HTL and with the various HTL combinations (Fe_3O_4, spiro-OMeTAD, and Fe_3O_4/spiro-OMeTAD). The steady-state PL spectra exhibited an emission peak centered at 760 nm of the CsFAMA perovskite (Fig. 5(a)). The deposition of Fe_3O_4, spiro-OMeTAD and

Fe_3O_4/spiro-OMeTAD HTLs lead to a 16, 94 and 95% drop in the PL intensity affirming the most efficient charge extraction with Fe_3O_4/spiro-OMeTAD in the case of the bilayer HTL. A slight blue shift in peak position was also observed possibly due to the filling of trap states. Fig. 5(a) inset demonstrates slightly better charge extraction by the bilayer HTL as compared to the pristine spiro-OMeTAD HTL. To confirm the charge extraction trends, we measured TRPL of all the films (Fig. 5(b)). The TRPL curves were fitted with a biexponential decay function $f(t) = A_1 \exp\left(\frac{-t}{\tau_1}\right) + A_2 \exp\left(\frac{-t}{\tau_2}\right)$ and average lifetime was calculated by $\tau_{ave} = \frac{\sum A_i \tau_i^2}{\sum A_i \tau_i}$ (see the summary of the fitting results in Table S2, ESI†).[43] Here, τ_1 and τ_2 indicate the fast decay component originated mainly from the quenching of charge carriers by the charge extraction layer as well as the defects in the perovskite film whereas the slow decay component is assumed to be mainly based on charge carrier relaxation due to radiative recombination, respectively. For this work, we emphasize on τ_1 as it enables us to compare the hole extraction *via* the different HTLs. The Fe_3O_4/spiro-OMeTAD bilayer HTL showed a fast decay of 1.03 ns with an amplitude of 98.5%, whereas the pristine spiro-OMeTAD layer exhibited a decay time of 1.55 ns with an amplitude of 92.17%. The smaller value of the fast decay component in the bilayer HTL confirms faster extraction of photogenerated charge carriers from the perovskite to the HTL when a thin Fe_3O_4 layer is employed. This is also evident from a faster charge extraction in the bilayer HTL (see the inset in Fig. 5(b)).

In order to investigate whether the inclusion of a thin Fe_3O_4 inter-layer changes the interfacial trap density, we performed space charge limited current (SCLC) measurements. We fabricated single carrier (hole only) devices with the configuration: ITO/Fe_3O_4/CsFAMA/spiro/WO_3/Ag and ITO/Fe_3O_4/CsFAMA/Fe_3O_4/spiro/WO_3/Ag to analyze the impact of the Fe_3O_4/spiro-OMeTAD double layer on trap density (n_t).

Fig. 5(c) and (d) depict the SCLC curves for the pristine spiro-OMeTAD and Fe_3O_4/spiro-OMeTAD bilayer HTL, respectively. The SCLC measurements can provide information on the conductivity trap density, and mobility of the thin films. The SCLC curve consists of three distinct regions that can be distinguished based on the value of exponent (n). The $n = 1$ region is the ohmic region (green line) where the conductivity (σ) of materials can be calculated. Charge carrier mobility can be calculated in the trap-free region when $n = 2$ (blue line) using Mott–Gurney's law ($\mu = \frac{8 J_D L^3}{9 \varepsilon \varepsilon_0 V^2}$).[40] For $n > 3$, the current rapidly increases due to the filling of traps (red line) and the trap density (n_t) is measured in this region using the formula $n_t = \frac{2 V_{TFL} \varepsilon \varepsilon_0}{e L^2}$ where V_{TFL} is the trap-filled limit voltage, L is the thickness of the absorber layer, ε is a dielectric constant whose value is 65 for the CsFAMA perovskite layer, ε_0 is the vacuum permittivity (8.8542×10^{-14} F cm^{-1}) and e is the charge (1.602×10^{-19} C). The calculated n_t for the Fe_3O_4/spiro-OMeTAD bilayer (1.30×10^{16} cm^{-3}) device was lower than that of the pristine spiro-OMeTAD (1.42×10^{16} cm^{-3}) counterpart suggesting lower traps due to probable defect passivation. The slightly reduced defect density in the bilayer HTL-based devices is also evident from the dark current measurements (Fig. S9, ESI†). The slightly lower dark current in the case of the Fe_3O_4/spiro-OMeTAD bilayer HTL suggests that the bilayer can prevent the leakage current, which is beneficial in improving the J_{SC}.

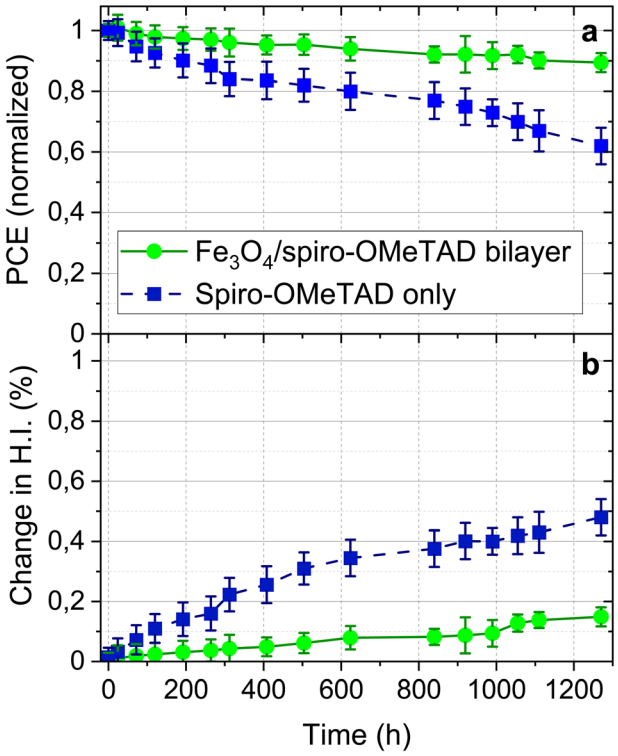

Fig. 6 Shelf-life stability of the PSCs. (a) Change in the PCE of the reference PSC (employing a spiro-OMeTAD HTL) and PSC employing a bilayer HTL (Fe_3O_4/spiro-OMeTAD). The error bars show the performance trends in at least three devices of each type. (b) Hysteresis index of the same devices.

We also investigated the shelf-life stability of the PSCs employing the bilayer HTL as well as the reference PSCs employing spiro-OMeTAD HTL only. The devices were stored in a dry chamber (R.H. below 3%) in the dark and measured using a J–V setup in an inert atmosphere. For reliability and a better comparison, the PCE trends of multiple devices from each type are shown in Fig. 6. Fig. 6(a) shows a 38% drop in the initial PCE of the reference PSC employing spiro-OMeTAD HTL only whereas the relative PCE drop in the device employing a bilayer HTL was only 11%. The change in the PCE is mainly governed by the changes in the FF and the V_{OC} of the devices, whereas the J_{SC} remains less effected over the entire measurement time. Given the identical storage and measurement conditions, these trends indicate that the different stability is linked to the intrinsic material properties, which in this study is the different HTL. To further understand the different stability trends in the devices, we also tracked the hysteresis

index (HI) over the entire stability testing period. An increase in the HI suggests deterioration in the device performance due to various internal (material related properties including interfaces) and external factors (*JV* scan conditions, pre-biasing, and atmospheric conditions, *etc.*). We note a drastic increase in the HI in the reference PSC to 0.48 ± 0.06 whereas the HI drop in the PSCs employing a bilayer HTL was around 0.15 ± 0.03. Since all the external factors in this experiment are identical, the change in the HI over time is attributed to the intrinsic material properties, which in our study is the different HLTs. The different HI FF and the V_{OC} trends in both devices suggest that the stability is mainly determined by the interfacial properties, which might lead to charge accumulation and diffusion of ions across the interface. One possible mechanism is the diffusion of volatile Li ions present in the spiro-OMeTAD HTL that are well-known to induce instability in the PSCs. Insertion of a smooth Fe_3O_4 layer restricts such a diffusion and thereby improves the device stability over time.

4. Conclusion

In summary, we fabricated regular planar triple cation perovskite solar cells using inorganic–organic double HTLs (Fe_3O_4/spiro-OMeTAD). A thin layer of Fe_3O_4 nanoparticles dispersed in toluene, a non-polar solvent, was deposited between the perovskite and spiro-OMeTAD. The Fe_3O_4 nanoparticles exhibited a dense layer of uniformly distributed nanoparticles on the perovskite layer. The Fe_3O_4/spiro-OMeTAD bilayer structure improved the photovoltaic performance of the PSC by enhancing hole extraction and transport resulting in suppressed recombination. Moreover, the formation of a uniform and smooth spiro-OMeTAD overlayer contributed to the enhanced stability of the perovskite solar cells, which is linked to reduction in ion migration across the perovskite/HTL interface upon insertion of a thin Fe_3O_4 layer. We also observed a significant decrease in trap densities of the modified bilayer devices. We propose that the modified bilayer HTL could be a promising alternative for further enhancement in the efficiency and environmental stability of triple cation perovskite solar cells.

Author contributions

AAQ performed the experimental work and wrote the first draft of the manuscript with inputs from all authors. E. S. assisted in device fabrication. AF supervised the experimental work and assisted in interpretation of the results with inputs from LSM. All authors contributed to the manuscript writing and were involved in the discussions. LSM and SJ oversaw the project progress and contributed to data analysis.

Conflicts of interest

There are no conflicts to declare.

Acknowledgements

The authors would like to thank Particle Analysis Center (for XRD) and Nanolab (for SEM measurements) of the University of Konstanz, Germany, and the Higher Education Commission (HEC), Islamabad, Pakistan, for their support.

References

1 S. S. Mali and C. K. Hong, p–i–n/n–i–p type planar hybrid structure of highly efficient perovskite solar cells towards improved air stability: synthetic strategies and the role of p-type hole transport layer (HTL) and n-type electron transport layer (ETL) metal oxides, *Nanoscale*, 2016, **8**(20), 10528–10540, DOI: 10.1039/C6NR02276F.
2 S. S. Shin, S. J. Lee and S. I. Seok, Metal Oxide Charge Transport Layers for Efficient and Stable Perovskite Solar Cells, *Adv. Funct. Mater.*, 2019, **29**(47), 1900455.
3 R. Singh, P. K. Singh, B. Bhattacharya and H.-W. Rhee, Review of current progress in inorganic hole-transport materials for perovskite solar cells, *Appl. Mater. Today*, 2019, **14**, 175–200.
4 H. S. Jung and N.-G. Park, Perovskite Solar Cells: From Materials to Devices, *Small*, 2015, **11**(1), 10–25.
5 N. Marinova, S. Valero and J. L. Delgado, Organic and perovskite solar cells: Working principles, materials and interfaces, *J. Colloid Interface Sci.*, 2017, **488**, 373–389.
6 N. J. Jeon, J. H. Noh, W. S. Yang, Y. C. Kim, S. Ryu, J. Seo and S. I. Seok, Compositional engineering of perovskite materials for high-performance solar cells, *Nature*, 2015, **517**(7535), 476–480.
7 J. Sala, M. Heydarian, S. Lammar, Y. Abdulraheem, T. Aernouts, A. Hadipour and J. Poortmans, Compositional Investigation for Bandgap Engineering of Wide Bandgap Triple Cation Perovskite, *ACS Appl. Energy Mater.*, 2021, **4**(7), 6377–6384.
8 NREL, https://www.nrel.gov/pv/assets/pdfs/pv-efficiencies-07-17-2018.pdf. Retrieved on 4.10.2018 2022, Retrieved on 8.8.2022.
9 A. F. Akbulatov, V. M. Martynenko, L. A. Frolova, N. N. Dremova, I. Zhidkov, S. A. Tsarev, S. Y. Luchkin, E. Z. Kurmaev, S. M. Aldoshin and K. J. Stevenson, *et al.*, Intrinsic thermal decomposition pathways of lead halide perovskites APbX3, *Sol. Energy Mater. Sol. Cells*, 2020, **213**, 110559.
10 J. Bisquert and E. J. Juarez-Perez, The Causes of Degradation of Perovskite Solar Cells, *J. Phys. Chem. Lett.*, 2019, **10**(19), 5889–5891.
11 J. Prakash, A. Singh, G. Sathiyan, R. Ranjan, A. Singh, A. Garg and R. K. Gupta, Progress in tailoring perovskite based solar cells through compositional engineering: Materials properties, photovoltaic performance and critical issues, *Mater. Today Energy*, 2018, **9**, 440–486.
12 S. Bi, X. Leng, Y. Li, Z. Zheng, X. Zhang, Y. Zhang and H. Zhou, Interfacial Modification in Organic and Perovskite Solar Cells, *Adv. Mater.*, 2019, **31**(45), 1805708.
13 S. Wu, R. Chen, S. Zhang, B. H. Babu, Y. Yue, H. Zhu, Z. Yang, C. Chen, W. Chen and Y. Huang, *et al.*, A chemically

inert bismuth interlayer enhances long-term stability of inverted perovskite solar cells, *Nat. Commun.*, 2019, **10**(1), 1161.

14 H. A. Dewi, J. Li, H. Wang, B. Chaudhary, N. Mathews, S. Mhaisalkar and A. Bruno, Excellent Intrinsic Long-Term Thermal Stability of Co-Evaporated $MAPbI_3$ Solar Cells at 85 °C, *Adv. Funct. Mater.*, 2021, **31**(22), 2100557.

15 R. Azmi, E. Ugur, A. Seitkhan, F. Aljamaan, A. S. Subbiah, J. Liu, G. T. Harrison, M. I. Nugraha, M. K. Eswaran and M. Babics, *et al.*, Damp heat-stable perovskite solar cells with tailored-dimensionality 2D/3D heterojunctions, *Science*, 2022, **376**(6588), 73–77.

16 L. Calió, S. Kazim, M. Grätzel and S. Ahmad, Hole-Transport Materials for Perovskite Solar Cells, *Angew. Chem., Int. Ed.*, 2016, **55**(47), 14522–14545.

17 A. Fakharuddin, M. Vasilopoulou, A. Soultati, M. I. Haider, J. Briscoe, V. Fotopoulos, D. Di Girolamo, D. Davazoglou, A. Chroneos and A. R. B. M. Yusoff, *et al.*, Robust Inorganic Hole Transport Materials for Organic and Perovskite Solar Cells: Insights into Materials Electronic Properties and Device Performance, *Sol. RRL*, 2021, **5**(1), 2000555.

18 E. H. Jung, N. J. Jeon, E. Y. Park, C. S. Moon, T. J. Shin, T.-Y. Yang, J. H. Noh and J. Seo, Efficient, stable and scalable perovskite solar cells using poly(3-hexylthiophene), *Nature*, 2019, **567**(7749), 511–515.

19 C. Redondo-Obispo, T. S. Ripolles, S. Cortijo-Campos, A. L. Álvarez, E. Climent-Pascual, A. de Andrés and C. Coya, Enhanced stability and efficiency in inverted perovskite solar cells through graphene doping of PEDOT:PSS hole transport layer, *Mater. Des.*, 2020, **191**, 108587.

20 P. Zhou, T. Bu, S. Shi, L. Li, Y. Zhang, Z. Ku, Y. Peng, J. Zhong, Y.-B. Cheng and F. Huang, Efficient and stable mixed perovskite solar cells using P3HT as a hole transporting layer, *J. Mater. Chem. C*, 2018, **6**(21), 5733–5737, DOI: 10.1039/C8TC01345D.

21 Q. Zhao, R. Wu, Z. Zhang, J. Xiong, Z. He, B. Fan, Z. Dai, B. Yang, X. Xue and P. Cai, *et al.*, Achieving efficient inverted planar perovskite solar cells with nondoped PTAA as a hole transport layer, *Org. Electron.*, 2019, **71**, 106–112.

22 G. Tumen-Ulzii, T. Matsushima and C. Adachi, Mini-Review on Efficiency and Stability of Perovskite Solar Cells with Spiro-OMeTAD Hole Transport Layer: Recent Progress and Perspectives, *Energy Fuels*, 2021, **35**(23), 18915–18927.

23 N. A. N. Ouedraogo, G. O. Odunmbaku, B. Guo, S. Chen, X. Lin, T. Shumilova and K. Sun, Oxidation of Spiro-OMeTAD in High-Efficiency Perovskite Solar Cells, *ACS Appl. Mater. Interfaces*, 2022, **14**(30), 34303–34327.

24 L. Nakka, Y. Cheng, A. G. Aberle and F. Lin, Analytical Review of Spiro-OMeTAD Hole Transport Materials: Paths Toward Stable and Efficient Perovskite Solar Cells, *Adv. Energy Sustainability Res.*, 2022, **3**(8), 2200045.

25 X. Liu, Y. Cheng, B. Tang, Z. G. Yu, M. Li, F. Lin, S. Zhang, Y.-W. Zhang, J. Ouyang and H. Gong, Shallow defects levels and extract detrapped charges to stabilize highly efficient and hysteresis-free perovskite photovoltaic devices, *Nano Energy*, 2020, **71**, 104556.

26 S.-G. Kim, T. H. Le, T. de Monfreid, F. Goubard, T.-T. Bui and N.-G. Park, Capturing Mobile Lithium Ions in a Molecular Hole Transporter Enhances the Thermal Stability of Perovskite Solar Cells, *Adv. Mater.*, 2021, **33**(12), 2007431.

27 Y. Liu, Y. Hu, X. Zhang, P. Zeng, F. Li, B. Wang, Q. Yang and M. Liu, Inhibited aggregation of lithium salt in spiro-OMeTAD toward highly efficient perovskite solar cells, *Nano Energy*, 2020, **70**, 104483.

28 M.-C. Jung and Y. Qi, Dopant interdiffusion effects in n–i–p structured spiro-OMeTAD hole transport layer of organometal halide perovskite solar cells, *Org. Electron.*, 2016, **31**, 71–76.

29 J. C. Yu, J. Sun, N. Chandrasekaran, C. J. Dunn, A. S. R. Chesman and J. J. Jasieniak, Semi-transparent perovskite solar cells with a cross-linked hole transport layer, *Nano Energy*, 2020, **71**, 104635.

30 T. H. Schloemer, T. S. Gehan, J. A. Christians, D. G. Mitchell, A. Dixon, Z. Li, K. Zhu, J. J. Berry, J. M. Luther and A. Sellinger, Thermally Stable Perovskite Solar Cells by Systematic Molecular Design of the Hole-Transport Layer, *ACS Energy Lett.*, 2019, **4**(2), 473–482.

31 T. H. Schloemer, J. A. Christians, J. M. Luther and A. Sellinger, Doping strategies for small molecule organic hole-transport materials: impacts on perovskite solar cell performance and stability, *Chem. Sci.*, 2019, **10**(7), 1904–1935, DOI: 10.1039/C8SC05284K.

32 J. Song, W. Hu, Z. Li, X.-F. Wang and W. Tian, A double hole-transport layer strategy toward efficient mixed tin-lead iodide perovskite solar cell, *Sol. Energy Mater. Sol. Cells*, 2020, **207**, 110351.

33 W. H. Nguyen, C. D. Bailie, E. L. Unger and M. D. McGehee, Enhancing the Hole-Conductivity of Spiro-OMeTAD without Oxygen or Lithium Salts by Using $Spiro(TFSI)_2$ in Perovskite and Dye-Sensitized Solar Cells, *J. Am. Chem. Soc.*, 2014, **136**(31), 10996–11001.

34 S.-K. Kim, H.-J. Seok, D.-H. Kim, D.-H. Choi, S.-J. Nam, S.-C. Kim and H.-K. Kim, Comparison of NiOx thin film deposited by spin-coating or thermal evaporation for application as a hole transport layer of perovskite solar cells, *RSC Adv.*, 2020, **10**(71), 43847–43852, DOI: 10.1039/D0RA08776A.

35 X. Miao, S. Wang, W. Sun, Y. Zhu, C. Du, R. Ma and C. Wang, Room-temperature electrochemical deposition of ultrathin CuOx film as hole transport layer for perovskite solar cells, *Scr. Mater.*, 2019, **165**, 134–139.

36 U. Er, K. C. Icli and M. Ozenbas, Spin-coated copper(I) thiocyanate as a hole transport layer for perovskite solar cells, *J. Solid State Electrochem.*, 2020, **24**(2), 293–304.

37 A. A. Mamun, T. T. Ava, T. M. Abdel-Fattah, H. J. Jeong, M. S. Jeong, S. Han, H. Yoon and G. Namkoong, Effect of hot-casted NiO hole transport layer on the performance of perovskite solar cells, *Sol. Energy*, 2019, **188**, 609–618.

38 B. A. Nejand, V. Ahmadi, S. Gharibzadeh and H. R. Shahverdi, Cuprous Oxide as a Potential Low-Cost Hole-Transport Material for Stable Perovskite Solar Cells, *ChemSusChem*, 2016, **9**(3), 302–313.

39 S. Xiao, F. Xu, Y. Bai, J. Xiao, T. Zhang, C. Hu, X. Meng, H. Tan, H.-P. Ho and S. Yang, An Ultra-low Concentration of

Gold Nanoparticles Embedded in the NiO Hole Transport Layer Boosts the Performance of p–i–n Perovskite Solar Cells, *Sol. RRL*, 2019, **3**(2), 1800278.

40 R. Li, P. Wang, B. Chen, X. Cui, Y. Ding, Y. Li, D. Zhang, Y. Zhao and X. Zhang, NiOx/Spiro Hole Transport Bilayers for Stable Perovskite Solar Cells with Efficiency Exceeding 21%, *ACS Energy Lett.*, 2020, **5**(1), 79–86.

41 J. Tirado, M. Vásquez-Montoya, C. Roldán-Carmona, M. Ralaiarisoa, N. Koch, M. K. Nazeeruddin and F. Jaramillo, Air-Stable n–i–p Planar Perovskite Solar Cells Using Nickel Oxide Nanocrystals as Sole Hole-Transporting Material, *ACS Appl. Energy Mater.*, 2019, **2**(7), 4890–4899.

42 R. Kaneko, H. Kanda, K. Sugawa, J. Otsuki, A. Islam and M. K. Nazeeruddin, Perovskite Solar Cells Using Surface-Modified NiOx Nanoparticles as Hole Transport Materials in n–i–p Configuration, *Sol. RRL*, 2019, **3**(9), 1900172.

43 G.-W. Kim, G. Kang, K. Choi, H. Choi and T. Park, Solution Processable Inorganic–Organic Double-Layered Hole Transport Layer for Highly Stable Planar Perovskite Solar Cells, *Adv. Energy Mater.*, 2018, **8**(26), 1801386.

44 A. Bag, R. Radhakrishnan, R. Nekovei and R. Jeyakumar, Effect of absorber layer, hole transport layer thicknesses, and its doping density on the performance of perovskite solar cells by device simulation, *Sol. Energy*, 2020, **196**, 177–182.

45 F. Ansari, M. Salavati-Niasari, O. Amiri, N. Mir, B. Abdollahi Nejand and V. Ahmadi, Magnetite as Inorganic Hole Transport Material for Lead Halide Perovskite-Based Solar Cells with Enhanced Stability, *Ind. Eng. Chem. Res.*, 2020, **59**(2), 743–750.

46 K. Wang, H. Ren, C. Yi, C. Liu, H. Wang, L. Huang, H. Zhang, A. Karim and X. Gong, Solution-Processed Fe_3O_4 Magnetic Nanoparticle Thin Film Aligned by an External Magnetostatic Field as a Hole Extraction Layer for Polymer Solar Cells, *ACS Appl. Mater. Interfaces*, 2013, **5**(20), 10325–10330.

47 W. Zhang, Y. Xu, H. Wang, C. Xu and S. Yang, Fe3O4 nanoparticles induced magnetic field effect on efficiency enhancement of P3HT:PCBM bulk heterojunction polymer solar cells, *Sol. Energy Mater. Sol. Cells*, 2011, **95**(10), 2880–2885.

48 M. Saliba, T. Matsui, J.-Y. Seo, K. Domanski, J.-P. Correa-Baena, M. K. Nazeeruddin, S. M. Zakeeruddin, W. Tress, A. Abate and A. Hagfeldt, *et al.*, Cesium-containing triple cation perovskite solar cells: improved stability, reproducibility and high efficiency, *Energy Environ. Sci.*, 2016, **9**(6), 1989–1997, DOI: **10.1039/C5EE03874J**.

49 J.-Y. Seo, S. Akin, M. Zalibera, M. A. R. Preciado, H.-S. Kim, S. M. Zakeeruddin, J. V. Milić and M. Grätzel, Dopant Engineering for Spiro-OMeTAD Hole-Transporting Materials towards Efficient Perovskite Solar Cells, *Adv. Funct. Mater.*, 2021, **31**(45), 2102124.